JETIR.ORG ISSN: 2349-5162 | ESTD Year : 2014 | Monthly Issue
JOURNAL OF EMERGING TECHNOLOGIES AND INNOVATIVE RESEARCH (JETIR)
An International Scholarly Open Access, Peer-reviewed, Refereed Journal

PV BASED ANN CONTROLLER FOR HALF-BRIDGE FULL-BRIDGE AC–DC CONVERTER FOR BI-DIRECTIONAL EV CHARGER

[1]Mr K.R. S.V. Durga Prasad, [2]T.Bhargavi
[1]PG scholar in the Dept. of Electrical & Electronics Engineering, Holy Mary Institute of Technology & Science, Bogaram (V), Medchal District, Hyderabad, India.
[2]Assistant Professor in the Dept. of Electrical & Electronics Engineering, Holy Mary Institute of Technology & Science, Bogaram (V), Medchal District, Hyderabad, India.

Abstract : This study presents a photovoltaic (PV) based artificial neural network (ANN) controller for a half-bridge/full-bridge AC–DC converter, designed for bi-directional electric vehicle (EV) charging applications. With the increasing demand for renewable energy integration and efficient EV charging solutions, the proposed controller aims to optimize power flow between the PV system, the grid, and the EV. The performance of an artificial neural network (ANN)-based control for a PV stand-alone system with DC/DC Boost converter topology and controller based on single-stage AC-DC resonant converter, without Electrolytic capacitors (E-cap), for bi-directional EV battery chargers is proposed in this paper. The topology is a Half-Bridge (HB)-Full-Bridge (FB) resonant converter with MOSFET's connected in series and in opposite direction on its AC Half-Bridge side plus an active filter on the DC-side. No use of E-cap makes the converter more reliable. The establishment of an appropriate control scheme enables a wide range of active and reactive power control under different AC and DC voltage levels. In addition, this controller is used as a supervisor to train the ANN, which is designed with the help of Matlab/Simulink software. Once the DC-link voltage is regulated. The proposed controller not only facilitates the converter to operate under Zero Voltage Switching (ZVS) for all switching instants, but also minimizes the conduction loss. ZVS allows higher switching frequencies and together with a reduction in conduction losses improves efficiency. The active filter is controlled to absorb the low frequency current ripple and prevent it from going to the battery. Charging the battery with reduced low frequency ripple prevents extra heat production and increases the lifespan of the battery.

IndexTerms **-** photovoltaic (PV), electric vehicle (EV), artificial neural network (ANN), Half-Bridge (HB)-Full-Bridge (FB) resonant, Zero Voltage Switching (ZVS).

I. INTRODUCTION

The transition to electric vehicles (EVs) is a critical step toward reducing greenhouse gas emissions and dependence on fossil fuels. As the demand for EVs continues to rise, so does the need for efficient and flexible charging solutions. Bi-directional EV chargers, which enable energy transfer both to and from the vehicle, are becoming increasingly important for smart grid applications, vehicle-to-grid (V2G) systems, and the integration of renewable energy sources. This study focuses on the development of a photovoltaic (PV) based artificial neural network (ANN) controller tailored for a half-bridge/full-bridge AC–DC converter, specifically designed for bi-directional EV charging applications. The proposed system addresses the challenges associated with traditional charging systems by optimizing power flow between the PV system, the electrical grid, and the EV's battery.

The number of Plug-in Electric Vehicles (PEVs) on the road is steadily increasing due to their appealing features, such as zero emissions. It is anticipated that they may soon fully replace conventional vehicles. Historically, the limited all-electric driving range and the scarcity of fast charging stations have hindered the widespread adoption of EVs. However, advancements in technology have extended the driving range, and the availability of fast charging stations has improved significantly. Despite this progress, the necessity for on-board Class II chargers remains, as they are integral to the vehicle's operation. These chargers must be compact, efficient, reliable, and lightweight. The primary function of an on-board charger is to charge the battery from the AC grid, typically accomplished using unidirectional converters. However, bi-directional chargers can perform additional functions, such as reactive power support and phase balancing. Furthermore, when considering a network of EVs connected to the grid, both grid operators and EV owners can benefit, as these vehicles can act as distributed energy storage systems. Bi-directional chargers also enable electrification of off-grid loads, a capability referred to as Vehicle-to-Home (V2H), which has garnered considerable research interest.

A suitable bi-directional charger must maintain power quality compliant with grid standards while efficiently performing power conversion across a wide range of battery voltages and currents, in accordance with battery charging algorithms. Additionally, it should limit high-frequency current ripple to the battery. Electrolytic capacitors (E-caps) are commonly used in charger topologies due to their high energy density, but their limited lifespan and impact on reliability pose challenges. Replacing E-caps

with more reliable film capacitors increases both cost and volume. One challenge in single-phase chargers is the low-frequency power ripple generated by these converters. This ripple, which can reach peak levels equivalent to the average power under a unity power factor, is often directed to the battery, causing additional heat due to the internal resistance. Moreover, if reactive power is present on the grid side, the battery current polarity can shift at the same frequency as the ripple, a phenomenon known as micro-cycle. Both excess heat generation and micro-cycles contribute to battery wear and reduce lifespan.

On-board bi-directional battery charger topologies can be classified into two main categories: i) single-stage converters and ii) two-stage converters. Generally, two-stage topologies consist of a front-stage boost converter for Power Factor Correction (PFC), followed by a DC-link and an isolated DC-DC converter for power control. Each stage can be controlled independently, simplifying control. However, this approach may require variable operating points for the AC-DC and DC-DC converters, potentially reducing overall efficiency.

In contrast, single-stage topologies require fewer components, resulting in a more compact and cost-effective design. While they offer lower losses when designed and controlled optimally, single-stage converters demand more complex design and control strategies compared to two-stage topologies. Research has explored single-stage topologies for both single-phase and three-phase applications. For instance, single-phase designs typically use 12 power switches, while three-phase variants require 16. In these configurations, low-frequency power is diverted to the battery.

DC-DC Dual Active Bridge (DAB) converters are utilized in automotive, aerospace, and telecommunications due to their high power density, isolation, soft-switching capabilities, and versatility across various voltage and power levels. Single-stage AC-DC DAB converters have been examined for bi-directional battery charging applications, with various control strategies proposed. For example, one study presented a single-stage HB-FB DAB converter, utilizing symmetric variable frequency and phase shift control. However, the direct derivation of control variables from voltage measurements can lead to poor dynamic performance and sensitivity to parameter variations.

Another approach employed a 3 × 3 dimensional look-up table for control optimization, relying heavily on transformer parameters. This method requires substantial data storage and is sensitive to variations, limiting its applicability. Further studies have investigated variable phase-shift and frequency modulation, but similar challenges regarding data dependency and storage remain. Recent work introduced an online control algorithm for AC-DC HB-FB DAB, which eliminates the need for look-up tables but still faces issues with double frequency power penetration into the DC side.

Given that bi-directional battery chargers must handle wide-ranging power and voltage fluctuations, a single-stage charger based on a DAB resonant converter emerges as a strong candidate, especially when optimally controlled. Previous research has proposed a single-stage DAB resonant converter, derived from a HB-HB resonant configuration that operates without E-caps and minimizes component count. This topology has been analyzed in detail, though dynamic performance assessments are still lacking in the existing literature.

Converter Topology and Design

The proposed converter utilizes a half-bridge (HB) and full-bridge (FB) resonant topology, where MOSFETs are configured in series and opposing directions on the AC side. This innovative arrangement allows for efficient switching and enhances the overall performance of the converter. One of the significant advantages of this design is the elimination of electrolytic capacitors (E-cap), which are typically used for energy storage in conventional designs. The absence of E-caps not only increases reliability by reducing the risk of failure but also improves the thermal management of the system, making it suitable for long-term applications.

Control Strategy

A robust control scheme is essential for maintaining the stability and efficiency of the converter under varying operational conditions. The ANN controller is trained using historical operational data to predict optimal control strategies, enabling real-time adjustments based on the dynamic characteristics of the PV output and load conditions. Using MATLAB/Simulink, the ANN model is developed to facilitate efficient regulation of the DC-link voltage, ensuring that the converter operates within desired voltage levels during both charging and discharging cycles.

Efficiency Enhancements

The implementation of Zero Voltage Switching (ZVS) is a key feature of the proposed controller, allowing the converter to operate with minimal switching losses at all switching instances. This capability is particularly beneficial at higher switching frequencies, which contribute to improved power density and overall system efficiency. By reducing conduction losses, the system can operate more effectively, providing a higher quality of power to the EV battery.

Active Filtering and Battery Longevity

To further enhance system performance, an active filter is integrated on the DC side to manage low-frequency current ripple. This filter is crucial for absorbing unwanted ripple currents that can negatively impact battery health and efficiency. By controlling these low-frequency components, the active filter prevents excessive heat generation during the charging process, thereby increasing the battery's lifespan and improving its reliability.

The proposed PV-based ANN controller for the half-bridge/full-bridge AC–DC converter represents a significant advancement in bi-directional EV charging technology. By optimizing power flow, enhancing efficiency through ZVS, and reducing thermal stress on the battery, this system supports the growing demand for sustainable energy solutions in the EV market. This research not only contributes to the development of more reliable and efficient charging systems but also underscores the importance of integrating intelligent control strategies in the pursuit of a sustainable energy future.

ANN-Based MPPT Controller:

The ANN approach utilizes historical data and real-time inputs to predict the MPP effectively.

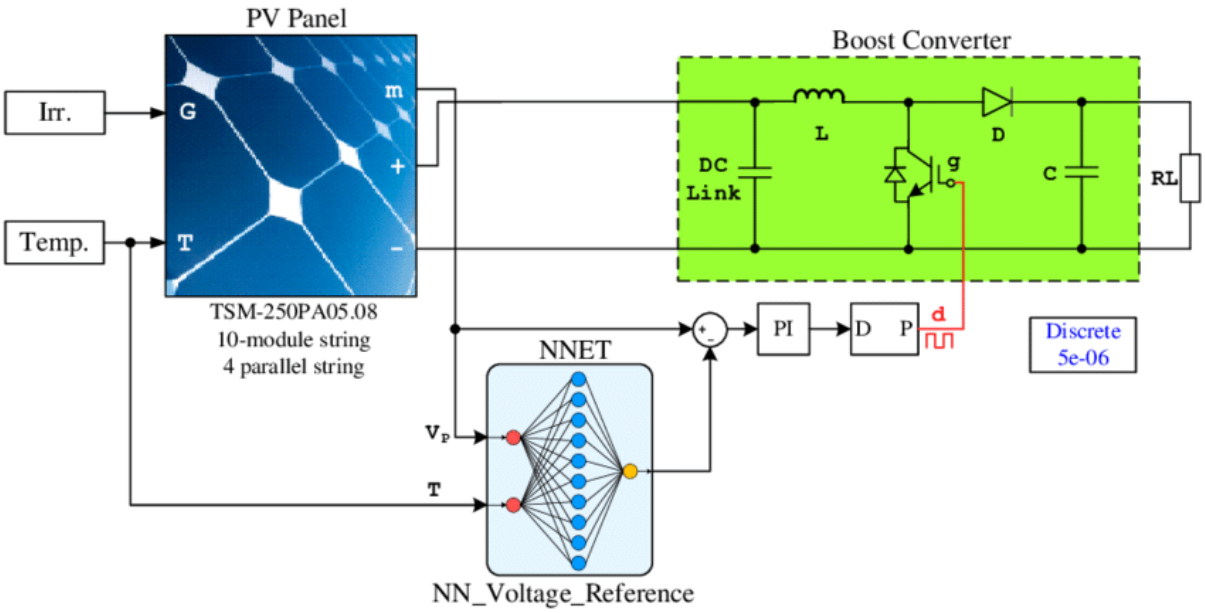

Fig1. ANN MPPT controller for the PV Boost converter.

ANN BASED MPPT

Artificial neural networks (ANNs) are a family of statistical learning models inspired by biological neural networks (the central nervous systems of animals, in particular the brain) and are used to estimate or approximate functions that can depend on many inputs and are generally unknown. Artificial neural networks are generally presented as systems of interconnected "neurons" which send messages to each other. The connections have numeric weights that can be tuned based on experience, making neural nets adaptive to inputs and capable of learning. [4] The ANN model is developed in MATLAB/Simulink environment. A feedforward based neural network with two neurons in input layer, five neurons in output layer and one in output layer is constructed. The model of network is as below.

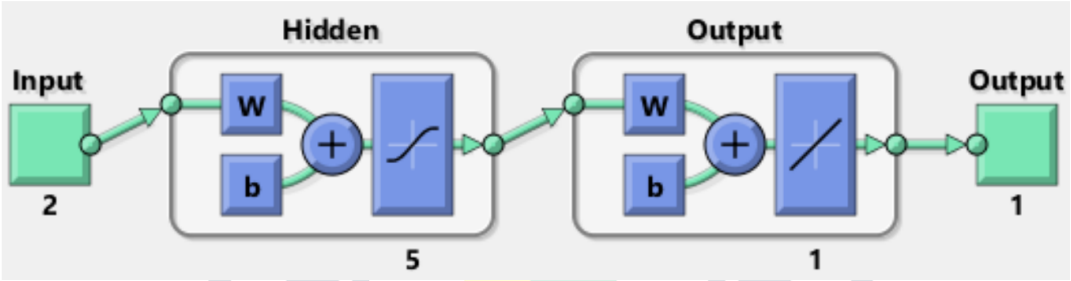

Fig.2 Neural Network Model

BOOST CONVERTER

A boost converter is like step up chopper i.e., used to step up the input voltage level. The basic circuit diagram for a Boost regulator using IGBT, when the IGBT (Insulated gate bipolar transistor) is on current flows through inductor and IGBT and energy gets stored in the inductor. Now when IGBT is turned off then energy previously stored in the inductor is released through capacitor and load. The amount by which the output voltage gets boosted up depends upon the duty ratio.

Duty ratio= $\frac{T_{ON}}{T_{ON}+T_{OFF}}$ k, and $Vo = \frac{V_{in}}{1-k}$= output voltage.

THE PROPOSED MPT METHOD FOR THE PMSG WTGS

II. ANN Based MPT Algorithm

The feed-forward ANN is meant to generate MPT connection with enhanced converter controller and favoured pitch attitude to the pitch actuator based on the investigated function curves. In popular, the structure of a multi-layer ANN accommodates an enter, hidden, and output layers, as depicted in Fig6. The neurons of the hidden layers with proper weights and activation functions make sure that information flows from input neurons to output neurons.

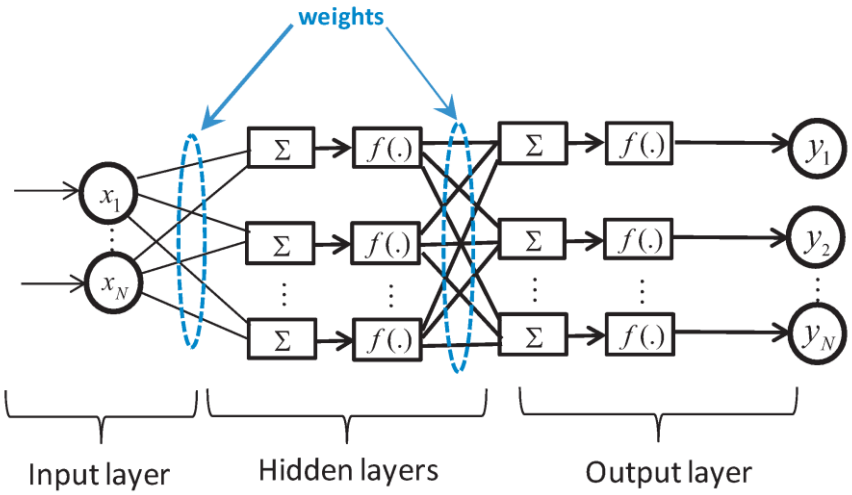

Fig3. ANN neural structure.

In order to create ANN block, we should first configure the WTGS gadget's input and output records. ANN block is educated to generate the right rotational speed reference by the use of the MPT method while maintaining the pitch angle null. When the PMSG WTGs reach their maximum power, the system should transfer to make certain the required pitch perspective for each input information on the way to keep away from the WTGs from being overloaded. The constructed feed-forward community contains one enter layer with neurons representing tidal velocity fluctuations and one output layer with neurons.

This starts with a small wide variety of hidden neurons and increases range of neurons. The neural network should then be taught and tested. The different types of hidden neurons are then raised, and previous layers are repeated until the training and checking the outputs to obtain optimal values. The Levenberg–Marquardt (LM) set of rules is used for training the ANN as soon as structure of neuro-controllers is adjusted[10]. LM set of rules is a variant of Newton's technique for decreasing capabilities which might be sums of squares of other nonlinear capabilities [11]. In order to minimise overall performance index, algorithm need to update the network settings as follows [12]:

Hessian matrix = $\nabla^2 F(X)$

$$\Delta X = [\nabla^2 F(X)]^{-1} \nabla F(X) \quad (17)$$

∇F(X) is a gradient.

Considering F(X) as the current index,

It is defined as below:

$$F(X) = \sum_{i=1}^{N} e_i^2(X) = e^T(X)\, e(X) \quad (18)$$

Gradient may be given as:

$$\nabla F(X) = 2J^T(X)e(X) \quad (19)$$

Jacobian matrix = J(X)

Here implementation of LM method necessitates construction of the Jacobian matrix with dimension proportionate to number of the training patterns[13].

Then, Hessian matrix can be uttered as in form of:

$$\nabla F(X) = 2J^T(X)J(X) + 2S(X) \quad (20)$$

And

$$S(X) = \sum_{i=1}^{N} e_i(X)\, \nabla^2 e_i(X) \quad (21)$$

An empirical comparison analysis has achieved the use of numerous checks on the way to pick a sufficient number of neurons within the buried layer. The performance of the utilised LM technique changed into evaluated via taking into consideration number of epochs and simply squared mistakes determined. The education process's overall performance for varying numbers of neurons within hidden layer. Training exams reveal that growing wide variety of neurons inside the hidden layer permits LM algorithm to achieve a lower optimization preventing criterion across a greater wide variety of epochs. When hi is greater than 10, the MSE rises, indicating that network can be overtrained using such patterns.

TOPOLOGY AND ANALYSIS

The proposed topology is shown in Fig. 1. In this topology, back-to-back MOSFETs are used on the AC-side HB to be able to chop the grid voltage whose polarity is changing. The gating signals for this configuration are shown in Fig. 2. The AC-side circuit chops the input AC voltage into high frequency AC voltage and applies it to the resonant circuit Transformer is for isolation. The DC-side has a FullBridge (FB) formed by MOSFETs that exchanges the energy between high frequency link and the DC-bus. A decoupling circuit in the DC-side filters out the low frequency power ripples to avoid them entering the battery. In continue, first the resonant circuit analysis is presented. Decoupling circuit analysis will come after.

RESONANT CIRCUIT ANALYSIS

As shown in Fig. 3(a) pulse-voltages v1 from the AC-side, and v2 and v3 from the battery-side, are applied to the resonant circuit. In this figure, Ll1, Ll2 and Lm are the leakage and magnetizing inductances of the transformer and R1, R2 are the winding resistances of the transformer. For the sake of effortlessness, all the resonant circuit variables at the right-hand side of the circuit (battery-side) such as v2 and v3 are being transferred to the left-hand side (AC-side) and the prime sign is used to show the transferred variable (v ′ 2 , v ′ 3). The circuit is shown in Fig. 3(b). Duty-cycles and phase-shifts are the control variables. At every switching period, T, duty cycles are promptly chosen to transfer the desired instantaneous power, pt, achieve ZVS for all the switching instants t0 to t5, and minimize the resonant RMS current. Fig. 4 shows different switching states of operation of the

resonant circuit and decoupling circuit during one switching period. Before starting the time domain analysis for once switching cycle we need to make some assumptions. The analysis of the circuit is done with the following assumptions:

• vCi and vCo, are constant during each switching cycle.

• All the resonant circuit variables (v1, v ′ 2, v ′ 3 and ires) are periodic with the frequency of fsw, which is the switching frequency.

• The dead times between upper and lower switches of each leg are very small compared to the period T and during those time intervals, the variation of vCres and ires is very small too.

• All the transformer parasitic are negligible.

• Lres and Cres are the equivalents inductance and capacitance of the resonant circuit after transferring the circuit to the AC-side.

Based on the assumptions made above, the time domain equations for all the time intervals shown in Fig. 4 ([ti, ti+1] , i = 0 − 5,t6 = T) can be derived. The close format of time equations for the two state variables of the resonant circuit, vCres and ires are shown in (1,2). In these equations, Ii and Vi are the initial values of the state variables for each interval as shown in (3,4). The natural frequency of resonant tank ωn is shown in (5). Variables ϕ and K change in each switching interval and they are shown in (6,7). v1i , v´2i and v´3i are the value of v1, v2 and v3 during i-th state ([ti, ti+1]).

$$v_{Cres}(t) = K\cos(\omega_n(t-t_i)+\varphi) + v_{1i} - v'_{2i} + v'_{3i}$$

$$i_{res}(t) = -K_i C_{res}\omega_n \sin(\omega_n(t-t_i)+\varphi)$$

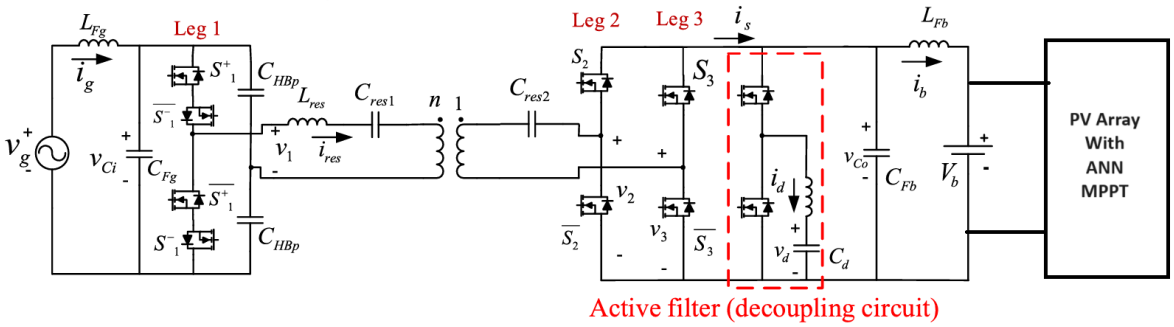

Fig4. Proposed Topology with PV ANN MPPT method

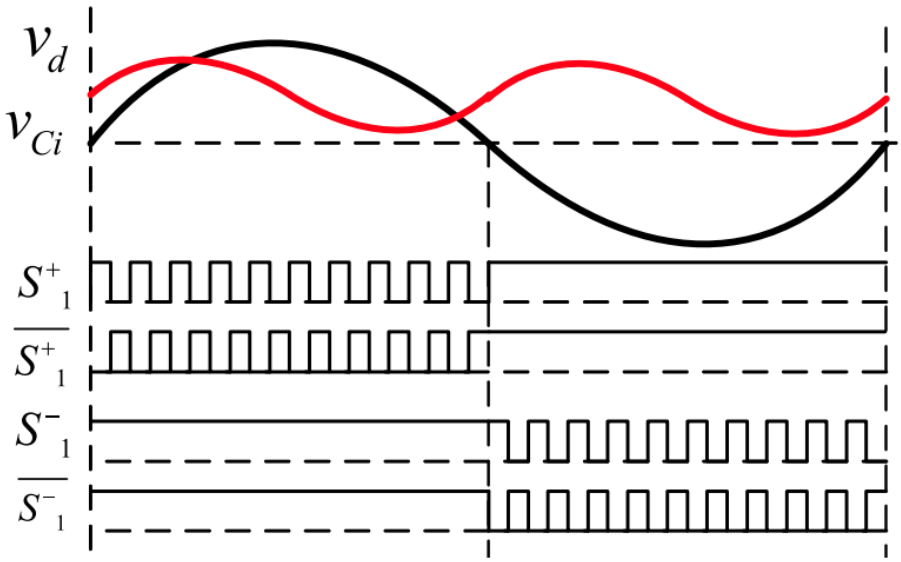

FIGURE 5. Gating signals for the AC-side Bridge.

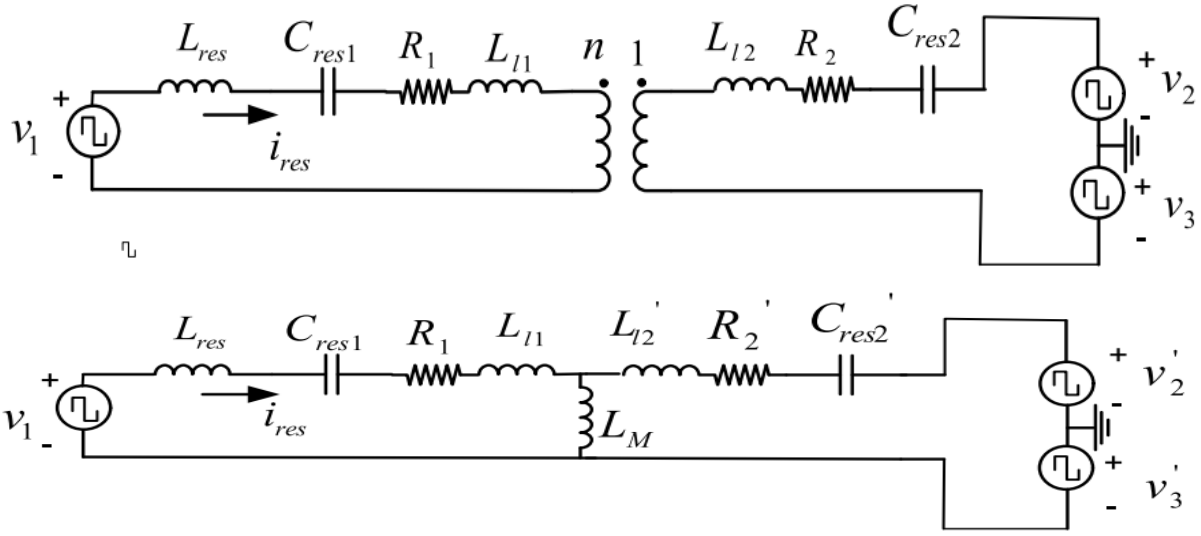

FIGURE 6. High-frequency resonant circuit: (a) circuit and (b) equivalent circuit with all the parameters referred to the primary-side.

$$i_{res}(t_i) = I_i$$
$$V_i = v_{Cres}(t_{i-1}) - v_{1i} + v'_{2i} - v'_{3i}$$
$$\omega_n = \frac{1}{\sqrt{C_{res}L_{res}}}$$
$$\varphi = \tan^{-1}\frac{-I_i}{V_i C_{res}\omega_n}$$
$$K_i = -sgn(\frac{I_i}{V_i})V_i\sqrt{1+(\frac{I_i}{V_i C_{res}\omega_n})^2}$$

The RMS current of resonant tank on the primary side over one switching cycle is presented with < ires > and it shown in (8). After replacing ires form (2) into (8) and some calculation, the closed form shown in (9) is obtained.

$$< i_{res} >^2 = \frac{1}{T}\sum_{i=0}^{i=5}\int_{t_i}^{t_{i+1}} i_{res}dt \qquad (8)$$

$$< i_{res} >^2 = \frac{(C_{res}\omega_n)^2}{T}\sum_{i=0}^{i=5}\int_{t_i}^{t_{i+1}} K_i^2\sin^2(\omega_n(t-t_i)+\varphi)\,dt$$

During the deadtime between the upper and lower switches of each leg, none of the switches of the leg are gated on. Fig. 5(a) shows an arbitrary leg j(j = 1,2,3 or d) during its deadtime. The current drawn from its midpoint is shown by ij . Based on this presentation, for leg1, i1 = ires, for leg 2 i2 = −nires, for leg 3, i3 = nires and for the decoupling leg, it is id . Fig. 5(b) shows the transient from bottom to top switch for leg j. In Mode I, the lower MOSFET is gated on, and it is conducting. Assuming in this transient, ij < 0 which is the necessary but not enough condition for ZVS transient, the current flow through the lower MOSFET. Right after Sj is gated off, the deadtime starts and snubber capacitances across the MOSFET's, as shown in Mode II, are charged, and discharged by this current. At time ti + tqi, Mode II ends and diode of the upper MOSFET conducts and clamp the upper switch voltage to zero and mode III start. The total gate charge for leg j, is denoted by Qtj. It depends on the leg voltage, vj which is equal to |vCi/2| for leg 1 and is equal to vCo for other legs. Current ij provides MOSFET gate charge during the deadtime in Mode II as shown in (10). Since ij is heavily enough inductive, it is not incorrect to assume it remains almost constant during the deadtime. This constant value is shown with Ii . Replacing this value in (10), yields (11).

$$Q_{\mathrm{tj}}(\mathrm{t}) = \int_{t_i}^{t} i_j dt, \forall t \in [t_i, t_i + t_{\mathrm{qi}}]$$
$$Q_{\mathrm{tj}}(v_j) = I_i t_{\mathrm{qi}}$$

To have full transition from lower to upper switch, in addition to the proper direction of Ij prior to the deadtime, current Ij should be large enough to provide the charge value of Qt(vj) during an interval tqi. This condition is shown in (12). For the second deadtime shown in Fig. 5(a), similar analysis can be done and its necessary condition for having ZVS is shown in (13).

$$I_i < -\frac{Q_{tj}(v_j)}{t_{qi}}$$
$$I_{i+1} > \frac{Q_{tj}(v_j)}{t_{q(i+1)}}$$

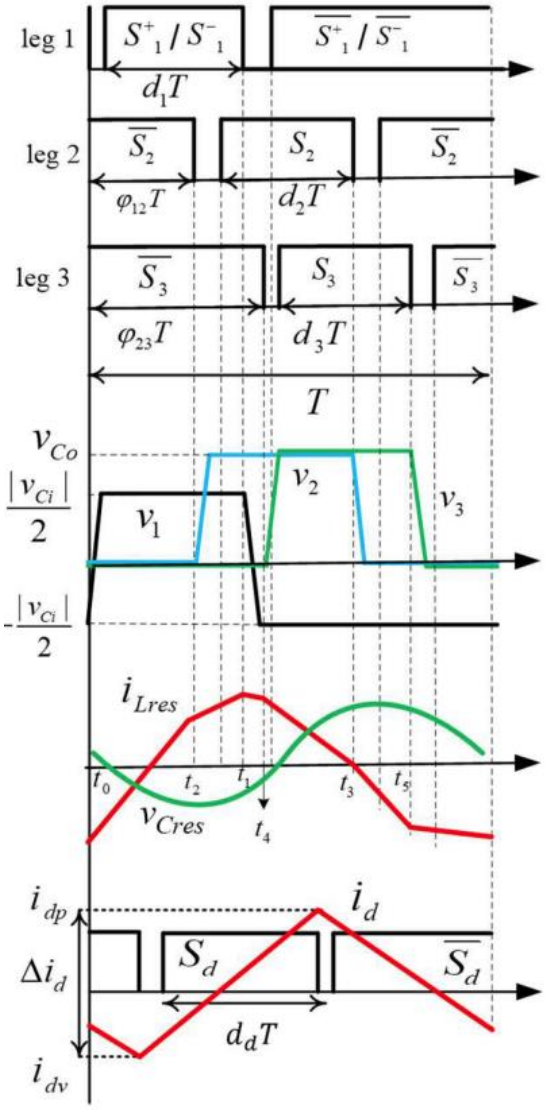

FIGURE 7. Different states of the resonant circuit and decoupling circuits.

Normally, due to small snubber capacitance and relatively highly inductive current of the resonant tank or decoupling circuit form one hand, and relatively smaller switching frequency from the other hand, the deadtimes can be neglected in analysis of the circuit in Fig. 4. Using time domain analysis of the circuit while dealing with variable phase shifts and duty cycles is not easy and requires a lot of calculation. Main harmonic Phasor analysis is a more simple and effective solution which have been used for resonant circuit analysis. In this paper, based on the assumptions made above, phasor analysis is applied to the circuit. The pulse voltages v1, v ′ 2 and v ′ 3 caused by switching actions in legs 1, 2 and 3 are shown in Fig. 6(a) where d1, d2 and d3 are the duty-cycles of the upper switch of each leg. ϕ12 is the phase-shift between the leg 1 and 2 and ϕ23 is the phase-shift between the leg 2 and 3. Let's assume y is a time domain variable in the resonant circuit. Then Y = |Y |∠ Y represents its phasor, where |Y | is its magnitude and∠ Y is its phase angle.

Fig. 6(b) shows the resonant circuit in the frequency domain. ω = 2πfsw is the angular switching frequency and as shown in (14), is the reactance of the resonant circuit at switching frequency fsw. To further simplify the analysis, all the phasor variables are presented in a per unit system, where VB, ZB, IB and PB are base values for voltage, impedance, current and power respectively and they are shown in (14). The inverted battery voltage transferred to the AC-side of the transformer, V ′ b , can be calculated from V ′ b = nVb. Defining f as f (d) = (1/π) √ 2(1 − cos(2πd)) helps to write the magnitude of the voltages in circuit Fig. 6(b) in a simpler way. For every vCi and vCo, V1 can be written as (16). pt , is the perunit power transferred through the resonant circuit in one switching cycle and can be written as (17).∠ Ires can be calculated form (17) and is shown in (18).

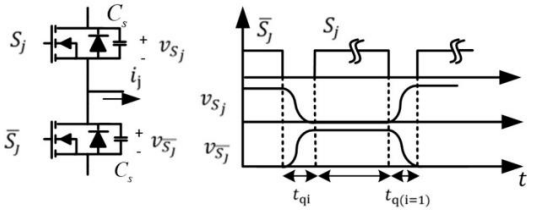

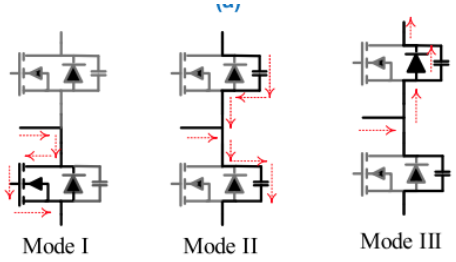

FIGURE 8. (a) deadtime transient for an arbitrary leg (b) deadtime related mode

$$X = L_{res}\omega - 1/C_{res}\omega$$

$$V_B = V_b', Z_B = X, I_B = V_b'/X, P_B = 0.5V_b'^2/X$$

$$\overline{V_1} = (v_{Ci}/V_b')f\ (d_1)\ \angle(-\pi d_1)$$

$$p_t = |\overline{V_1}||\overline{I_{res}}|\ cos(-\pi d_1 - \angle\overline{I_{res}})$$

$$\angle\overline{I_{res}} = -\pi d_1 - \ cos^{-1}(p_t/(|\overline{V_1}||\overline{I_{res}}|))$$

(19) shows the time expression of resonant current

$$i_{res}\ (t) = I_B\ |\overline{I_{res}}|\ \ cos\ (\omega t + \angle\overline{I_{res}})$$

) |V′ | in (20) is obtained by writing a KVL in Fig. 6(b). Equation (21) is obtained by substituting (17) in (20)

$$\left|\overline{V'}\right| = \sqrt{|\overline{I_{res}}|^2 + |\overline{V_1}|^2 - 2|\overline{V_1}|\ (|\overline{I_{res}}|)\ \sin\ (-\pi d_1 - \angle\overline{I_{res}})}$$

$$\left|\overline{V'}\right| = \sqrt{|\overline{I_{res}}|^2 + |\overline{V_1}|^2 - 2\sqrt{(|\overline{V_1}|\ |\overline{I_{res}}|)^2 - p_t^2}}$$

1) Achieving ZVS at all six switching instants t0 − t5, shown in Fig. 4(a), is very important. The deadtimes of leg 1, tq1 and tq2 should be kept below the value tqleg1max shown in which is 5% of the maximum ‘‘ON’’ time of the switches of leg 1. The marginal current for leg 1, Ileg1, which is the lower limit for the absolute value of the resonant current is therefore determined by placing tqleg1max in (12) and is shown in (23). Equation (19) shows the time expression of resonant current. From this equation, required conditions to achieve ZVS for leg I are found and shown in (24) and (25).

$$t_{qleg1max} = 0.05T.\max(d_1, 1-d_1)$$

$$I_{leg1} = Q_t(v_{Ci})/t_{qleg1max}$$

$$I_B\ |\overline{I_{res}}|\ \ cos\left(\angle\overline{I_{res}}\right) < -I_{leg1}$$

$$I_B\ |\overline{I_{res}}|\ \ cos\left(2\pi d_1 + \angle\overline{I_{res}}\right) > I_{leg1}$$

Equation (19) can be used to find the ZVS conditions for the switching instants related to FB circuit too. To have the ‘‘deadtime’’ of leg i (i=2,3,d), tqi, below the value tqlegjmax in (26) that is 5% of the maximum switches ‘‘on time’’ in each leg, the marginal current for leg j, Ilegi is given by (27). Based on these values, ZVS conditions are calculated and presented in (28)-(31

$$t_{qlegjmax} = 0.05T.\ \max\ (d_i,\ 1 - d_i)\ , i = 2,\ 3$$

$$I_{lej} = \frac{nQ_t(v_{Co})}{t_{qlegjmax}} j = 2,\ 3,\ d$$

$$I_B\ |\overline{I_{res}}|\ \cos\ \left(2\pi\varphi_{12} + \angle\overline{I_{res}}\right) > I_{leg2}$$

$$I_B\ |\overline{I_{res}}|\ \cos\ \left(2\pi\varphi_{12} + 2\pi d_2 + \angle\overline{I_{res}}\right) < -I_{leg2}$$

$$I_B\ |\overline{I_{res}}|\ \cos\ \left(2\pi\varphi_{12} + 2\pi\varphi_{23} + \angle\overline{I_{res}}\right) < -I_{leg3}$$

$$I_B\ |\overline{I_{res}}|\ \cos\ \left(2\pi\varphi_{12} + 2\pi d_2 + 2\pi\varphi_{23} + \overline{I_{res}}\right) < -I_{leg3}$$

(31) An important equation relates the |V′ | and FB parameters which are d2, d3 and ϕ23. To complete this equation, the origin is shifted from t = 0 to t = 2πϕ23. The new equation for V′ on is shown in (32). Since the shift in origin does not change the magnitude of the phasor, V′ remains unchanged and can be calculated from (32) as shown in (33). M is a new variable that represents the angle of V′ when the origin is shifted to t = 2πϕ23. Both |V′ |, shown in (33), and M, shown in (34) are only functions of FB param.

$$\overline{V'}$$

$$= \mathrm{f}\ (d_2)\ \angle(-\pi d_2) - \mathrm{f}\ (d_3)\ \angle(-\pi d_3 - 2\pi\varphi_{23})$$

$$\left|\overline{V'}\right|$$

$$= \sqrt{|\overline{V_2}|^2 + |\overline{V_3}|^2 - 2\ |\overline{V_2}|\ |\overline{V_3}|\cos\ (\pi\ (d_2 - d_3) + 2\pi\ (\varphi_{23}))}$$

$$= \tan^{-1}\ \frac{(-\mathrm{f}\ (d_2)\ \sin\pi d_2 + \mathrm{f}\ (d_3)\ \sin\ (\pi d_3 + 2\pi\varphi_{23}))}{(\mathrm{f}\ (d_2)\ \cos\pi d_2 - \mathrm{f}\ (d_3)\ \cos\ (\pi d_3 + 2\pi\varphi_{23}))}$$

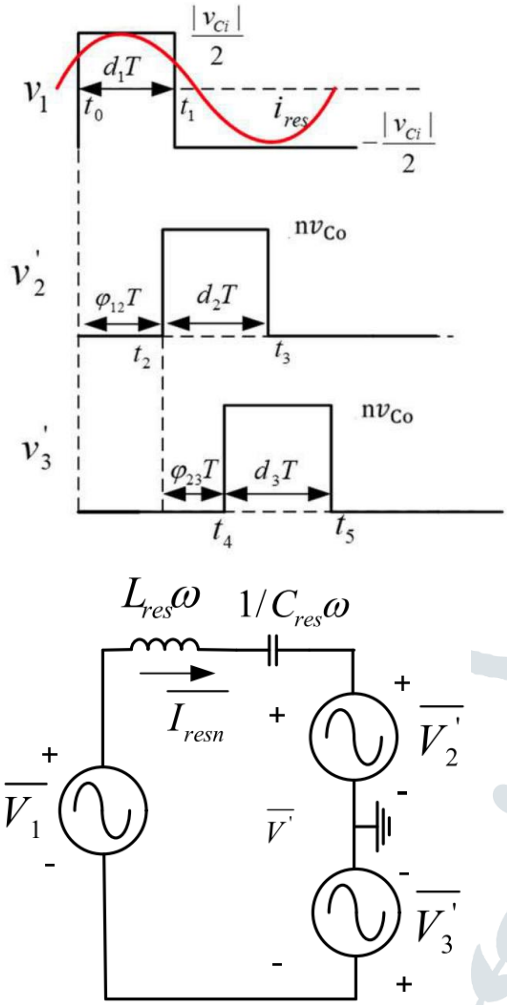

FIGURE 9. Circuit chosen for phasor analysis: (a) Pulse voltages applied to the resonant circuit. (b) Resonant circuit in phasor.

B. DECOUPLING CIRCUIT ANALYSIS

The shunt-active filter connected across the output filter capacitor acts like a buck converter and transfers the low-frequency AC power bi-directionally between the DC bus and decoupling capacitor, Cd. The decoupling circuit inductor is Ld and its current id is shown in Fig. 1. It is assumed that the active filter operates with the same switching frequency as the resonant circuit. To analyze the active filter, it is assumed that the voltage vCo and vd , remain constant during the switching period T. The inductor current variation, 1id can be calculated as.

$$\Delta i_d = (v_{Co} - v_d)\, v_d / (2fL_d v_d)$$

(35) As shown in Fig. 4, the decoupling current id has a triangular shape. Its peak and valley during each switching cycle, idp and idv can be calculated as (36) and (37). These peak and valley values vary from one switching to the other switching cycle.

$$i_{dp} = C_d \frac{dv_{Co}}{dt} + 0.5\Delta i_d$$

$$i_{dv} = C_d \frac{dv_{Co}}{dt} - 0.5\Delta i_d$$

(37) Given the grid voltage and grid current, vg and ig which are shown in (38)-(39), the power transferred from the grid, pg, can be derived and it is shown in (40). The angular frequency of the grid, ωg, is related to the grid frequency, fg, by ωg = 2pif.

$$v_g = V_m \cos(\omega_g t)$$

$$i_g = I_m \cos(\omega_g t + \theta_g)$$

$$p_g = P_m \cos(\theta) + P_m \cos(2\omega_g t + \theta_g)$$

This power has an AC component with the frequency of 2ωg and a DC component. In an ideal situation, all the AC component will go to the decoupling capacitor. Based on this assumption, (41) expresses the relationship between vd and the AC power component pac. Using (40) and (41), the time expression for vd can be deriven as shown in (42

$$v_d = \sqrt{v_{d0}^2 + 2C_d \int p_{ac}(t)dt}$$

$$v_d = \sqrt{v_{d0}^2 + P_m C_d \omega_g \left[\sin(2\omega_g t + \theta) - \sin(\theta_g)\right]}$$

2) In order to be able to absorb the maximum possible low frequency power at any battery voltage, vd need to be able to have the maximum possible variation. To have this, vd0 is set so that vd oscillates around its mid input voltage which is vCo 2. A control mechanism for ensuring maximum variation around vCo 2 is developed and will be presented in control select.

CONTROLLER

To be operated as a battery charger, the converter requires to exchange power with the grid at the point of common coupling. This power exchange should satisfy power quality standards, while covering a wide range of battery and grid voltage variations. In addition, active and reactive power demands enforced from the upper-level controller, which is VMS (Vehicle Management System), should be achieved. Furthermore, the low frequency power ripple should be absorbed by the active filter. To achieve all these tasks, the controller shown in Fig. 7 is proposed. The supervisory controller communicates with VMS and translates the commands into P and Q. The grid controller can be a closed loop PR controller. At first, resonant circuit controller which is an online search algorithm using limited stored data is presented. Then decoupling circuit controller will be describe, .

A. RESONANT CIRCUIT CONTROLLER

The most important part of the proposed converter is the resonant circuit controller. The voltages across bridges, vCi and vCo, with the desired instantaneous power, p ∗ t , are the inputs to this controller. For every set of inputs, the controller finds the optimal control vector u T = [d1ϕ12d2d3ϕ23] and sends it to the PWM unit as shown in Fig. 7. This optimal control vector transfers the desired power p ∗ t in the following switching cycle, while minimizes the RMS current for the resonant converter, and guaranties ZVS for all switches. Finding an analytical solution for u T is very complex since it, if achievable, is the solution to a nonlinear multi-variable optimization problem with unequal constraints. Numerical methods can be used to solve this problem, but they cannot be run online, as it takes a too long time for the controller to solve them. The numerical methods can be run offline r. saved in the memory, and then recalled. But, to have a decent resolution, this solution requires a large memory. The solution proposed here is to break the calculations down into two parts. One part is done online, while the other part that requires much less memory to store the result data would be done offline. The time spent for online calculations in this case is acceptable due to the proper choice of variables representing the operating point of the resonant converter. In addition, the offline calculations need to be done once only, and would not require a large memory space. The online algorithm is shown in Fig. 8. According to this figure, after receiving the input signals, p ∗ t , vCi and vCo, first per unitization of the inputs is done in the controller to simplify the calculations. The base values for voltage, current, power and impedance are shown in (14).

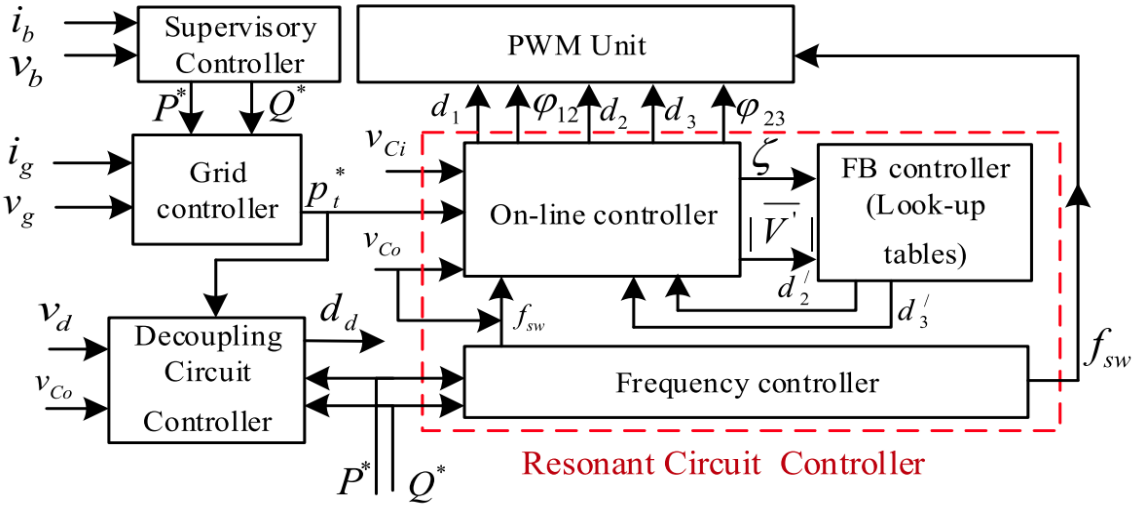

FIGURE 10. Proposed controller with dedicated resonant circuit controller.

The flowchart in Fig. 8 has 4 nested loops. The loop for the per-unitized magnitude of the resonant current, |Ires|, is called I-loop here. In I-loop |Ires| is set to Istart first and then in each iteration step the loop variable is increased by 1I until it reaches its final value Iend . Istart and 1I determine the search time and accuracy of the search. The smallest value for |Ires| is IMin given in (43). To ensure that Istart > IMin, Istart is selected based on (44). In addition, this range enables controller to adjust the start point using the information of the optimum point found in the previous calculation cycle, Iold , ith an adjustable coefficient, kI that is usually between 0 and 1. If kI = 0, then Istart = IMin and if kI = 1,then the search starts from the previous operating point. The former option can lead to an overly long calculation time and the later choice can cause the algorithm to miss the new optimal operating point, if any, since the new operating point might occur before the old operating point.

$$I_{Min} = \frac{|p_t^*|}{V_{1Max}} = \frac{2}{\pi}|p_t^*|$$

$$I_{start} = Max(I_{Min}, k_I I_{old})$$

4) After choosing Istart , the minimum value for the d1 can be calculated from (25). Then, in the d1-loop, the initial value for d1, which is d1start is selected, and then in each iteration step the loop variable is increased by 1d1 until it reaches its final value d1end . This initial value, d1start , can be selected based on the old operating point, d1old . The coefficient kd1 between 0 to 1 is used to choose the start value shown in .

$$d_1 = k_{d1} d_{1old}$$

Now, the value of |V1| can be calculated from (16). If this value is larger than its minimum possible value, V1Min, the algorithm will go to the next stage. V1Min is obtained from the power transfer equation in (17), when the cosine term is equal to 1, and is given in (46).

$$V_{1\text{Min}} = |p_t| / |\overline{I_{res}}|$$

In the next step, the algorithm calculates the angle of the resonance current,∠ Ires, from (18), as shown in (47). Based on (47), there are two solutions for∠ Ires,. The algorithm should try both to find the true answer.

$$\angle \overline{I_{res}} = -\pi d_1 \mp \cos^{-1}\left(2p_t / (|\overline{V_1}||\overline{I_{res}}|)\right)$$

Both solutions should be examined. In the algorithm they are labelled by ‘‘option I’’, and ‘‘option II’’. Only ‘‘option I’’ is explained here and depicted in detail in the flowchart of Fig. 8. The same procedure should be carried on for ‘‘option II. The algorithm first calculates V' form (20), which is simply a KVL in the resonant circuit loop. The algorithm checks to see if the value of V' is smaller than its maximum possible value given in (48) and obtained when d2, d3 and ϕ23 are set to 0.5.

$$V'_{Max} = 4/\pi$$

The algorithm then checks the ZVS conditions for the leg 1. In this manner, if the candidate (I, d1) does not gratify ZVS, the algorithm examines achieving ZVS for the next candidate, and skips any further calculations, and saves calculating times considerably that can be dedicated to other candidates. When a ZVS is detected, the algorithm starts inner loops, d2-loop and d3-loop. These loops sweep variables d2 and d3 with the step of 1d2 and 1d3 from their start values d2start and d3start to their end values d2end and d3end respectively. In the outer loops, I-loop and d2-loop, the old values for Ires and d1 are being used to choose an appropriate starting point value to reduce the repetition and calculation time. This assumption is valid since these variables and in particular Ires vary continuously in one cycle of the line voltage. For the FB parameters, this might not be correct. Therefore, different approach is used to choose the initial values for these loops. These initial values, shown in (49), are chosen using d'_2 and d'_3 that are named ‘‘approximated FB-side ZVS conditions’’ and will be discussed soon. Coefficients kd2 and kd3, similar to kd1 and kI, and are used to define the searching neighbourhood around d'_2 and d'_3. These coefficients control both the search time and the accuracy of the results

$$d_{2start} = k_{d2} d'_2,\ d_{3start} = k_{d3} d'_2$$

After choosing the initial values, the algorithm calculates the ϕ23,which synthesizes V' . The calculation is shown in (50) and (51). As shown, two options for ϕ23 exist and the controller should consider them both.

$$\varphi_{23} = \frac{1}{2\pi} \cos^{-1} \frac{|\overline{V_2}|^2 + |\overline{V_3}|^2 - |\overline{V'}|^2}{2\,|\overline{V_2}|\,|\overline{V_3}|} - 0.5\,(d_2 - d_3)$$

$$\varphi_{23} = -\frac{1}{2\pi} \cos^{-1} \frac{|\overline{V_2}|^2 + |\overline{V_3}|^2 - |\overline{V'}|^2}{2\,|\overline{V_2}|\,|\overline{V_3}|} - 0.5\,(d_2 - d_3)$$

For each option, ZVS conditions for the FB-side legs, legs 2 and 3, should be checked. As soon as ZVS conditions are satisfied, then the controller breaks from all the loops and delivers the operating point to the PWM unit. Since the outer loop starts from the smallest Ires , the first operating point that satisfies the ZVS conditions is in fact the optimal operating point. Fig. 9 depicts the searching area of the main resonant controller and its searching direction.

Results

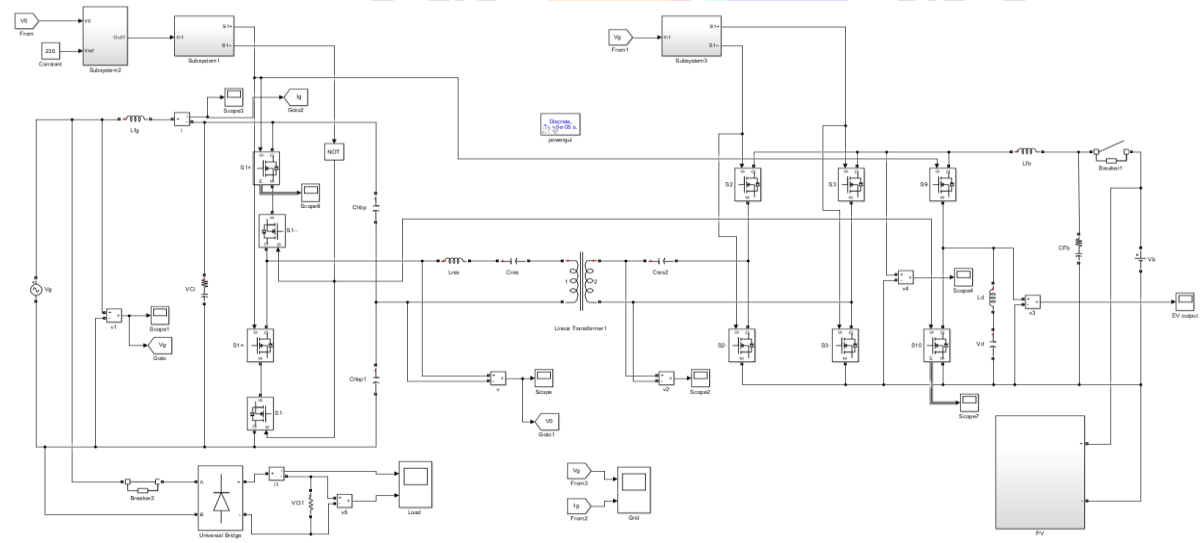

Fig11 Matlab Schematic Diagram of the Proposed system.

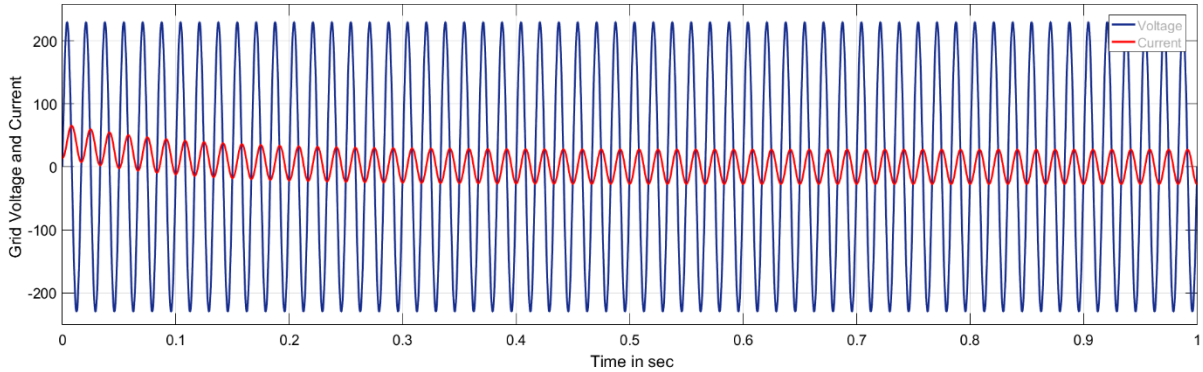

Fig12 Converter operation in G2V for Pm = 800 W , Vb = 350 V , Vg = 200 V θg = 0 Rad and fs = 100 kH

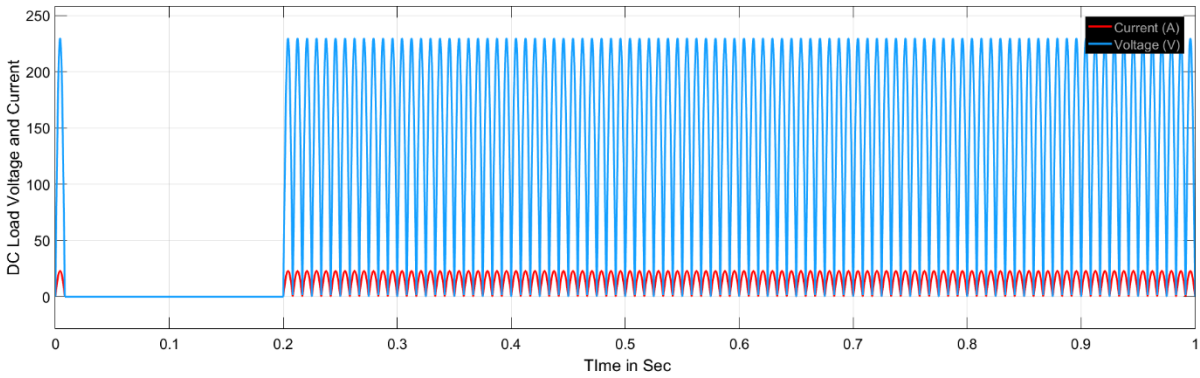

Fig13. Operation of the converter while load changes from Pm = 170 VA to 250VA for θg = π 12 Rad, Vb = 100 V, Vg = 180 V and fs = 120kHz.

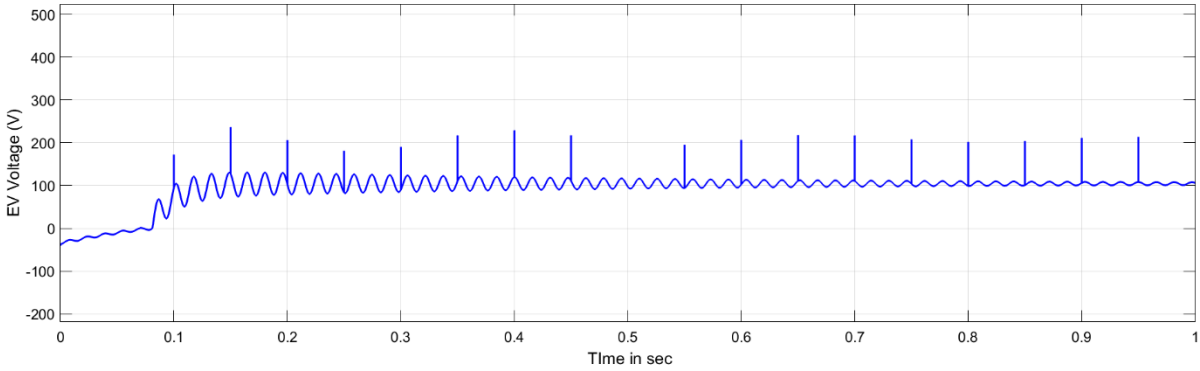

FIGURE 14. Resonant circuit waveforms in G2V when Pm = 800 W, Vb = 100 V , Vg = 200 V,θg = 0 Rad and fs = 100 kHz.

Conclusion

This study presents a photovoltaic (PV) based artificial neural network (ANN) controller for a half-bridge/full-bridge AC–DC converter, specifically designed for bi-directional electric vehicle (EV) charging applications. The proposed controller effectively addresses the challenges associated with traditional charging systems by optimizing power flow between the PV source, the grid, and the EV's battery. The use of an ANN enhances the control strategy by enabling real-time adaptation to changing environmental conditions, thereby improving the system's responsiveness and efficiency. The implementation of Zero Voltage Switching (ZVS) not only minimizes switching losses but also allows for higher operational frequencies, which contributes to the overall efficiency of the charger. Furthermore, the active filtering capabilities of the system significantly reduce low-frequency current ripple, protecting the battery from excess heat generation and prolonging its lifespan. The elimination of electrolytic capacitors enhances the reliability of the converter, making it more suitable for long-term applications.

In summary, the proposed PV-based ANN controller demonstrates a promising approach for optimizing bi-directional EV charging. By effectively integrating renewable energy sources with intelligent control mechanisms, this research contributes to the advancement of sustainable energy solutions in the electric vehicle market, paving the way for more efficient and reliable charging systems. Future work can focus on further refining the control algorithms and exploring additional enhancements to improve dynamic performance and adaptability under varying operational conditions.

REFERENCES

[1] M.YilmazandP.T.Krein,‘‘Reviewofbatterychargertopologies,charging power levels, and infrastructure for plug-in electric and hybrid vehicles,’’ IEEE Trans. Power Electron., vol. 28, no. 5, pp. 2151–2169, May 2013, doi: 10.1109/TPEL.2012.2212917.

[2] F. Musavi, M. Craciun, D. S. Gautam, W. Eberle, and W. G. Dunford, ‘‘An LLC resonant DC–DC converter for wide output voltage range battery charging applications,’’ IEEE Trans. Power Electron., vol. 28, no. 12, pp. 5437–5445, Dec. 2013, doi: 10.1109/TPEL.2013.2241792.

[3] M. Pahlevaninezhad, P. Das, J. Drobnik, P. K. Jain, and A. Bakhshai, ‘‘A ZVS interleaved boost AC/DC converter used in plug-in electric vehicles,’’ IEEE Trans. Power Electron., vol. 27, no. 8, pp. 3513–3529, Aug. 2012, doi: 10.1109/TPEL.2012.2186320.

[4] S. Li, J. Deng, and C. C. Mi, ‘‘Single-stage resonant battery charger with inherent power factor correction for electric vehicles,’’ IEEE Trans. Veh. Technol., vol. 62, no. 9, pp. 4336–4344, Nov. 2013, doi: 10.1109/TVT.2013.2265704.

[5] M.Ramezani and S.M. Madani, ‘‘A new zero voltage switching bridgeless PFC using an improved auxiliary circuit,’’ IET Power Electron. J., vol. 4, no. 6, pp. 732–741, Jul. 2011.

[6] C.-J. Shin and J.-Y. Lee, ‘‘An electrolytic capacitor-less bi-directional EV on-board charger using harmonic modulation technique,’’ IEEE Trans. Power Electron., vol. 29, no. 10, pp. 5195–5203, Oct. 2014, doi: 10.1109/TPEL.2013.2293781.

[7] A. M. Rahimi, ‘‘A lithium-ion battery charger for charging up to eight cells,’’ in Proc. IEEE Vehicle Power Propuls. Conf., Chicago, IL, USA, Sep. 2005, pp. 131–136, doi: 10.1109/VPPC.2005.1554545.

[8] H. L. Chan, ‘‘A new battery model for use with battery energy stor age systems and electric vehicles power systems,’’ in Proc. IEEE Power Eng. Soc. Winter Meeting. Conf., Singapore, Jan. 2000, pp. 470–475, doi: 10.1109/PESW.2000.850009.

[9] H. Wang and F. Blaabjerg, ‘‘Reliability of capacitors for DC-link applications in power electronic converters—An overview,’’ IEEE Trans. Ind. Appl., vol. 50, no. 5, pp. 3569–3578, Sep. 2014, doi: 10.1109/TIA.2014.2308357.

[10] A. Ristow, M. Begovic, A. Pregelj, and A. Rohatgi, ‘‘Development of a methodology for improving photovoltaic inverter reliability,’’ IEEE Trans. Ind. Electron., vol. 55, no. 7, pp. 2581–2592, Jul. 2008, doi: 10.1109/TIE.2008.924017.

Authors Details:

Mr K.R. S.V. Durga Prasad received a B-Tech degree in Electrical and Electronics Engineering at B V Chalamaiah Institute of Technology and Science, Bhatlapalem (v), Amalapuram(M), E.G.Dist, A.P. ,India from Jawaharlal Nehru Technological University kakinada and pursuing M-Tech in Power Electronics at Holymary Institute of Technology and Science, Bogaram(V), Medchal(D), Hyderabad, Telangana, India from Jawaharlal Nehru Technological University Hyderabad. Email ID: krsvdprasad@gmail.com, Contact No:7993953987

T.Bhargavi received B.Tech Degree in Electrical and Electronics Engineering from NOVA Institute of Science and Technology J.N.T.U. Hyderabad in 2017. And an M.Tech in Power Systems from Holy Mary Institute of Technology and Science in 2021. She had teaching experience of 4 years. Now working as an assistant professor at Holy Mary Institute of Technology and Science(Autonomous), Bogaram, Keesara, Medchal (Dist), Telangana, India E-Mail ID:bhargavitmanu@gmail.com, Contact No.:8099997829